# Deciphering the Origins of Transient Seismic Moment Accelerations by Realistic Dynamic Rupture Simulations

Julien Renou[*1,2], Martin Vallée[1], and Hideo Aochi[3,4]

## ABSTRACT

**Properties of earthquake source physics can be inferred from the comparison between seismic observations and results of dynamic rupture models. Although simple self-similar rupture models naturally explain the space and time observations at the scale of the whole earthquake, several observational studies based on the analyses of source time functions (STFs) suggest that they are unable to reproduce the initial accelerating phases of the rupture. We here propose to reproduce the observed transient moment accelerations, without affecting the global self-similarity of the rupture, to constrain their possible physical origins. Simulated STFs are generated from dynamic simulations with heterogeneous slip-weakening distance $D_c$. Heterogeneity is introduced on the fault plane through a fractal number-size distribution of circular patches, in which $D_c$ takes a value proportional to their radius. As a consequence of the stochastic spatial distribution of the patches, rupture development exhibits a large variability, and delays between initiation and main rupture activation frequently occur. This variability, together with the dynamic correlation between rupture velocity and slip velocity inside each broken patch, successfully perturbs the self-similar properties: rather than growing quadratically with time, STFs have an higher apparent time exponent, close to the observed value of 2.7. In a broader perspective, our simulations show that to respect observed STF shapes, realistic dynamic models should generate bursts of seismic moment, most likely by episodes where slip and rupture velocity are correlated. Such a behavior appears to emerge more naturally when considering heterogeneities in the friction parameters rather than in the initial stress.**

## KEY POINTS

- We explore the dynamic origins of high-frequency radiated energy observed in earthquake source time functions.
- Observations are explained by fault models with hierarchical patches and size-dependent fracture energy.
- Realistic dynamic models should include physical mechanisms correlating the slip and rupture velocities.

## INTRODUCTION

Continuous development of seismic networks in the last decades has vastly increased the number of seismic records, for earthquakes of different sizes occurring in all tectonic contexts. Analysis of these seismic observations are important as they can be compared with synthetics generated by dynamic source models, with the aim of improving realism of rupture scenarios. One of such observation-derived products are the teleseismic source time functions (STFs), which describe the time evolution of the seismic moment rate. Teleseismic STFs can be efficiently extracted for earthquakes of magnitude larger than 5.5–6, resulting in hundreds of observed STFs each year. Several STF catalogs have been built (Tanioka and Ruff, 1997; Bilek *et al.*, 2004), the most exhaustive today being the SCARDEC catalog (Vallée *et al.*, 2011; Vallée and Douet, 2016). STFs can be used to quantify global source parameters, such as duration, stress drop, and rupture velocity (Courboulex *et al.*, 2016; Chounet and Vallée, 2018; Chounet *et al.*, 2018). These latter studies for instance show that total seismic moment is proportional to the cube of the duration, or that stress drop and rupture velocity are magnitude independent, which together satisfy the assumption of self-similarity (Aki,

1. Institut de Physique du Globe de Paris, CNRS, Université de Paris, Paris, France, https://orcid.org/0000-0002-9860-0623 (JR); https://orcid.org/0000-0001-8049-4634 (MV); 2. Department of Earth Sciences, University of Oxford, Oxford, United Kingdom; 3. Laboratoire de Géologie, Ecole Normale Supérieure, PSL Research University, Paris, France, https://orcid.org/0000-0001-9405-9596 (HA); 4. Bureau des Recherches Géologiques et Minières, Orléans, France

*Corresponding author: julienrenou3@gmail.com

**Cite this article as** Renou, J., M. Vallée, and H. Aochi (2022). Deciphering the Origins of Transient Seismic Moment Accelerations by Realistic Dynamic Rupture Simulations, *Bull. Seismol. Soc. Am.* **XX**, 1–12, doi: 10.1785/0120210221

1967). The concept of self-similarity requires that all nondimensional quantities (e.g., slip over length or rupture velocity over wave velocity) are indeed constant. In this case, no clues about the earthquakes' magnitude can be found before rupture starts declining and moment rate steadily evolves as $t^2$ in the growing phase (Kostrov, 1964; Sato and Hirasawa, 1973).

Dynamic rupture simulations based on slip-weakening friction law (Ida, 1972) reproduce not only the rupture behaviors of earthquakes (Olsen *et al.*, 1997), but also such global self-similar relations by incorporating scaling laws in the friction parameters or in the initial stress field (Cocco *et al.*, 2009; Nielsen *et al.*, 2016; Gallovič *et al.*, 2019; Ulrich *et al.*, 2019; Aochi and Twardzik, 2020). For example, Aochi and Ide (2004) numerically show that linear increase of the friction parameter $D_c$ with distance to the rupture initiation, supported by observational evidence of growing $D_c$ with the final earthquake size (Abercrombie and Rice, 2005; Lancieri *et al.*, 2012), results in a rupture process with constant rupture velocity when the initial stress field is uniform. For scale-invariant $D_c$ under the same uniform initial stress, rupture velocity beyond the nucleation zone gradually increases throughout the rupture propagation and finally exceeds shear-wave velocity, which violates rupture self-similarity. Dynamic models with heterogeneous initial stress and constant $D_c$ also lead to self-similar relations for global source parameters, such as constant apparent stress drop or final seismic moment being proportional to the cube of the corner frequency (Ripperger *et al.*, 2007; Mai *et al.*, 2018; Aso *et al.*, 2019).

Although the STF is an integral view of the rupture process, preventing the direct analysis of local space–time features, time dependence of the moment rate provides insights on the earthquake rupture development. STFs can thus be used as a constraint for physics-based earthquake source modeling (Ulrich *et al.*, 2019; Wollherr *et al.*, 2019). Based on STFs analysis, recent studies (Meier *et al.*, 2016; Denolle, 2019; Danré *et al.*, 2019) identify distinct transient phases during the rupture process, and Renou *et al.* (2019) aimed at characterizing how rupture accelerates. The results of the latter study show that, despite magnitude-independent values, seismic moment acceleration does not respect steady self-similar growth: rather than evolving quadratically with time, STFs have a larger apparent time exponent (2.7), indicating that some source parameters such as rupture velocity or slip velocity do not behave independently when rupture accelerates. It is expected that the time exponent is equal to 2 in the case of steady self-similar growth of STF, corresponding to the linear increase of $D_c$ with hypocentral distance (Aochi and Ide, 2004). It therefore implies that different $D_c$ distributions are necessary to perturb the moment rate evolution when rupture accelerates.

The objective of the present study is to find possible origins of these transient moment accelerations by creating dynamic models whose heterogeneities of the friction parameter $D_c$ generate local source complexities. We use the model of Ide and Aochi (2005) as it already reproduces some important observed features. First, the fractal number-size distribution of circular patches generates a magnitude-independent behavior, in agreement with a large number of studies (Meier *et al.*, 2016; Okuda and Ide, 2018; Ide, 2019; Renou *et al.*, 2019). This universal rupture growth is explained by the cascading rupture of successive patches of growing sizes, with no information about the final size before rupture declines. Second, the hierarchical dependence of $D_c$ as a function of the patch size generates the observed self-similar global source properties (Aochi and Ide, 2004). Based on this framework, we perform dynamic rupture propagation on a number of random $D_c$ distribution maps. We then explore how heterogeneous $D_c$ affects the relationship between local rupture velocity and slip velocity, and in turn influences the resulting seismic moment accelerations. The role of an heterogeneous initial stress, combined with the $D_c$ heterogeneity, is finally investigated.

## MULTISCALING HETEROGENEOUS $D_c$ MODEL

### Slip-weakening friction law and numerical method

Because the effects of geometrical or structural complexities are not explored here, we consider a simple 2D planar fault configuration within a homogeneous elastic medium (Fig. 1a). Fault is a square grid of 64 × 64 points surrounded by an unbreakable barrier, with shear stress applied to one direction on the fault ($x$ axis in Fig. 1a). Slip is governed by slip-weakening friction law at each grid point (Fig. 1b), and its direction is the same as the direction of the applied shear stress. In this model, when shear stress $\tau$ increases from the initial stress $\tau_0$ and reaches the peak strength $\tau_y$, a critical slip distance $D_c$ is required to decrease $\tau$ to the residual stress $\tau_r$ to trigger dynamic slip instability. The energy per unit area provided to reach $D_c$ is the fracture energy $G_c$ and is proportional to $D_c$ when $\tau$ decreases linearly (see green area in Fig. 1b). For the simulations hereafter, $\tau_y$ and $\tau_0$ are kept constant so that $D_c$ or $G_c$ can be indifferently referred to as friction parameters.

Parameters of the slip-weakening friction law are then included in the formulation of the dynamic problem as boundary and initial conditions. Following the work of Aochi and Ide (2004), we solve the elastodynamic equations relating the stress and particle velocity with the boundary integral equation method (Fukuyama and Madariaga, 1998; Aochi *et al.*, 2000). The multiscaling approach of Aochi and Ide (2004), based on a renormalization technique, is used to model dynamic propagation regardless of the size of the rupture process, through a set of four subspaces with different physical scales. For each subspace, numerical problem is solved on a 64 × 64 spatial grid. Rupture first nucleates with abrupt stress drop on a finite crack in the subspace with the smallest physical dimensions, but this artificial initial effect is not visible after two renormalizations. When rupture reaches the edge of a subspace, renormalization is applied and rupture propagates into the subspace of larger physical dimensions. During each renormalization, the slip

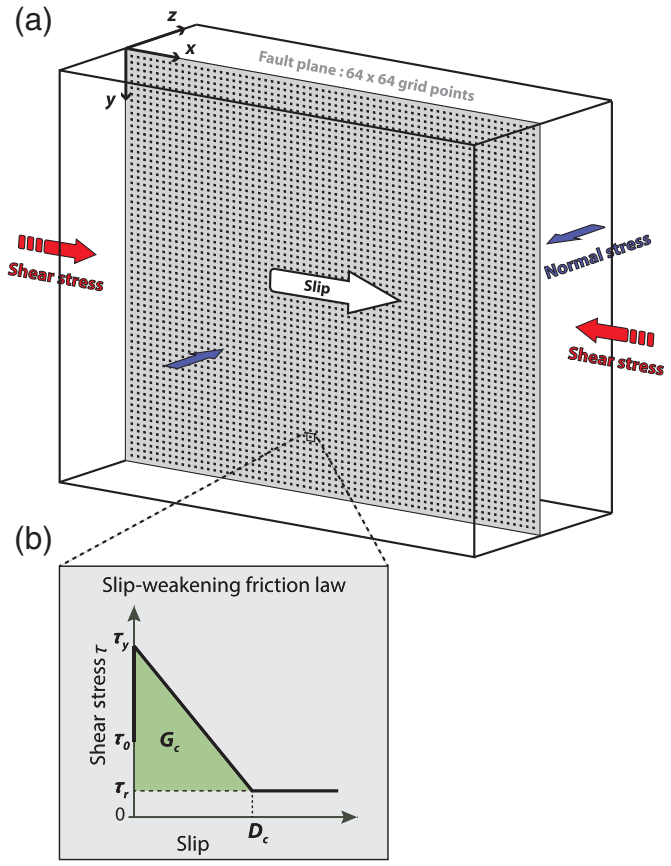


**10** **Figure 1.** (a) Fault configuration used in this study. A 2D planar fault composed of 64 × 64 points is embedded in a homogeneous elastic medium. Shear stress is applied in one direction and slip is restricted to the same direction. Normal stress is kept constant during the simulation. Physical dimensions of the fault plane are 65.536 km × 65.536 km. (b) Slip-weakening law governing the slip at each grid point. The fault is uniformly loaded at initial stress $\tau_0$ before the rupture. The slip-weakening distance $D_c$ is required to lower the stress from the peak strength $\tau_y$ to the residual stress $\tau_r$. The fracture energy $G_c$ is the energy per unit area required to reach $D_c$.

rate (namely, seismic moment release rate) and the fracture energy on the equivalent surface are always conserved (Aochi and Ide, 2004). As in the heterogeneous fault of Ide and Aochi (2005), large events develop over the evolving field in which the representative value of $D_c$ becomes large as the rupture grows. Very small values of $D_c$ disappear due to the homogenization during the renormalization. In such a model, rupture is macroscopically controlled by the large $D_c$ values and small heterogeneities with small $D_c$ become invisible in terms of seismic wave radiation, because the rupture front (cohesive zone) is predominantly governed by the largest $D_c$ values representing the scale of interest (Aochi and Ide, 2004).

This procedure enables us to continuously follow how a smaller event grows into a larger one and is consequently well-suited for our following analysis focusing on transient features of the rupture process. The procedure itself is nondimensional and we set such that the largest ruptures propagate into the last fourth subspace with dimensions of 65.536 km × 65.536 km, grid spacing of 256 m and timestep $dt = 0.0844$ s. The rigidity $\mu$ is equal to 32.4 GPa and the $P$- and $S$-wave velocities are $V_P = 6.0$ kms$^{-1}$ and $V_S = 3.46$ kms$^{-1}$, respectively.

## Fractal $D_c$ distribution of circular patches

Irregularities in terms of friction parameters are incorporated following the approach of Ide and Aochi (2005). We consider asperities as randomly distributed circular patches, with their number-size distribution following a fractal distribution. $N_n$ and $r_n$, the number and radius of the $n$th-order patches, are expressed as

$$N_n = 2^{-Dn} N_0 \quad \text{and} \quad r_n = 2^n r_0, \tag{1}$$

with $D = 2$ is the fractal dimension, and $N_0$ and $r_0$ are the number and radius of the smallest zero-order patches, respectively. As mentioned in the Introduction, global self-similarity of the rupture process arises from the linear grow of $D_c$ with $r_n$. The critical slip-weakening distance $D_{cn}$ of the $n$th-order patches can therefore be written as

$$D_{cn} = 2^n D_{c0}, \tag{2}$$

with $D_{c0}$ is the slip-weakening distance of the zero-order patches.

A random realization based on this procedure is shown in Figure 2. Fault heterogeneity map has the same physical dimension as the largest subspace of the numerical scheme (i.e., 65.536 km × 65.536 km) but is initially composed of 4096 × 4096 elements. We assume eight orders of patches and set values in equations (1) and (2) to $N_0 = 16,384$, $r_0 = 90$ m, and $D_{c0} = 1$ mm for smallest patches, leading for $n = 7$ to a single patch ($N_7 = 1$) with $r_7 = 11.52$ km and $D_{c7} = 128$ mm. These values are based on the parametrization previously done in Ide and Aochi (2005). Points belonging to several patches take the smallest $D_c$-value of these patches and we assign a large "background" $D_{c\max}$ (equal to 512 mm) to the points outside of all patches. Uniform $\tau_y = 5$ MPa and $\tau_r = 0$ MPa are assigned while $\tau_0 = 3$ MPa is kept constant so that the potential effects of an heterogeneous initial stress field are not considered here (see the Effects of a Random Initial Stress Field section). Complexity in the following simulations are therefore only caused by heterogeneous $D_c$.

As multiscaling simulation is done on 64 × 64 spatial grids for each of the four subspaces, the initial fault heterogeneity map has to be resampled according to the subspace physical dimension (Fig. 3). The subspace with the smallest physical dimensions has the same discretization as the initial map of $D_c$ (one value each 16 m) whereas in subspaces with larger physical dimensions, $D_c$ values are averaged to be consistent with the 64 × 64 spatial grids. Rupture artificially initiates in a stress-free region (i.e., with a peak strength

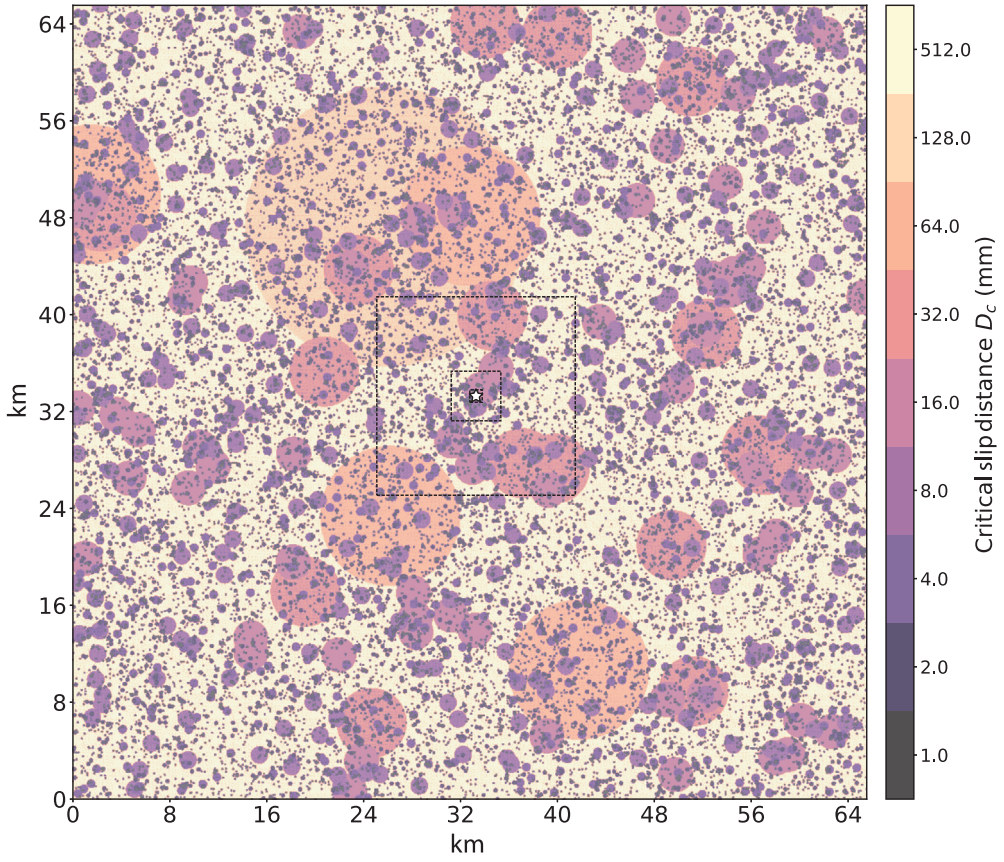


**Figure 2.** Fault heterogeneity map from random circular patches position, initially composed of 4096 × 4096 elements. The number of circular patches follows a fractal number-size relation. The value of $D_c$ is assigned on each patch following equations (1) and (2). The white star is the location of the artificial rupture initiation and the subspaces with growing physical dimensions are represented by dotted squares.

$\tau_y = 0$ MPa) of 60 m radius within a random zero-order patch in the middle of the fault and this nucleation procedure is performed for a large number of random heterogeneity maps. As a consequence of the fractal properties on the fault plane, most of the simulations stop within zero-order patches and only a few random $D_c$ distributions result in ruptures propagating in the largest patches, in agreement with the Gutenberg–Richter law (Ide and Aochi, 2005).

## EXPECTED CHARACTERISTICS OF THE MODEL

This multiscale heterogeneous configuration is by design a cascade model in which small and large events are the result of successive ruptures of increasing patch sizes. Growing phases of the largest events include characteristics of the smaller ones, resulting in a magnitude-independent rupture process as long as rupture develops.

During its development, rupture randomly hits areas with relatively high density of small and moderate-size patches, or on the contrary areas where the large $D_c$ values dominate. In the former case, rupture is expected to accelerate due to the relation between $D_c$ (or $G_c$) and rupture velocity $V_r$ (velocity at which the rupture front arrives at a grid point). In the dynamic case of a crack with a constant stress drop, fracture mechanics at the tip imposes that crack extension force $G$ is governed by the equation of motion $G_c = G$. As $G$ is a decreasing function of $V_r$ (Kostrov, 1966; Eshelby, 1969; Freund, 1972), energy balance requires that $V_r$ increases when $G_c$ decreases. The reciprocal argument implies that rupture is slowed down (or even arrested) when suddenly entering in areas with large $D_c$ values. Areas broken at fast rupture velocity are further expected to have a higher slip velocity (higher slip rate). This is illustrated by the quasi-dynamic self-similar circular crack model (Kostrov, 1964; Madariaga, 1976; Kaneko and Shearer, 2014), in which slip velocity at a given point and time behind the rupture front increases with rupture velocity. Heterogeneous $D_c$ is therefore expected to create bursts of seismic moment rate, by generating rupture episodes with joint increase of slip and rupture velocity. In the following, we explore how this model is actually able to reproduce the observations, by focusing on the events propagating over several scales of the fault model.

## RUPTURE CHARACTERISTICS IN HETEROGENEOUS $D_c$ MODELS

### Observed influence of $D_c$ on rupture velocity and slip velocity

In the study of Ide and Aochi (2005), one heterogeneity map is used to produce many simulations. However, we find that moderate-to-large earthquakes are similar as they are controlled only by one or few large patches and this does not guarantee sufficient variation for the purpose of study. We run 40 random heterogeneity maps, and we extract the largest events that naturally stop before reaching the borders of the fault model (20 typical simulations out of 40 are shown in Fig. 4). Such events offer the potential to both track their development phase and their macroscopic properties, the latter being consistently self-similar, as for instance the magnitude-duration scaling law shown in Figure S1, available in

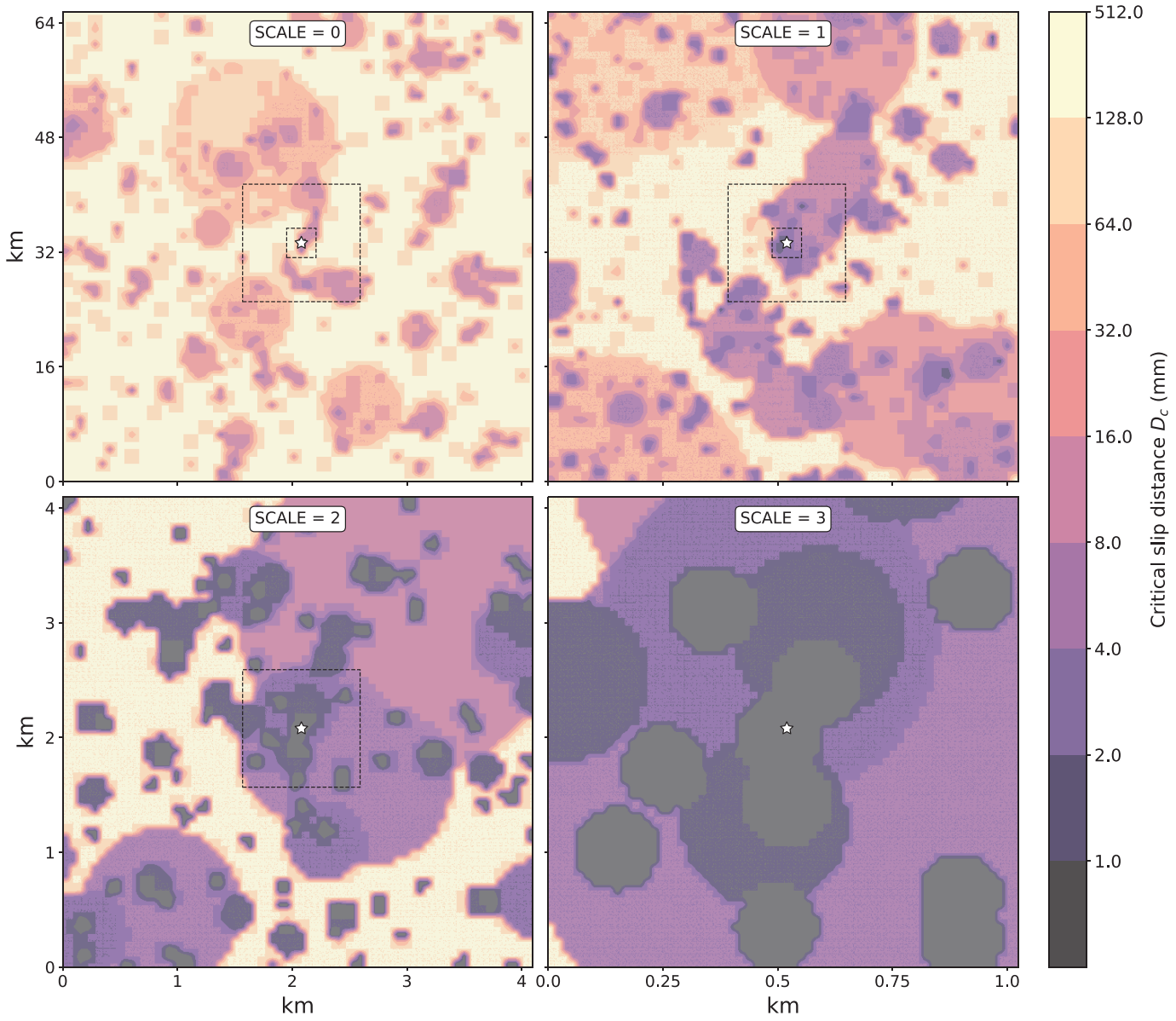


**Figure 3.** Example of the four subspaces, renormalized from one random realization shown in Figure 2, used for the multiscaling model. All the tested events start in the scale 3 (bottom right) of smallest dimension and possibly grow up to the scale 0 (top left). When present, the scales of smaller dimension are shown by dotted squares. The white star shown at all scales is the rupture initiation. All the events analyzed in this study propagate in the four subspaces.

the supplemental material to this article. As we are interested in the effect of $D_c$ on local source properties, Figure 4 also shows the iso–time contours of the rupture front.

Heterogeneous $D_c$ distribution generates complex and irregular ruptures, with different space–time evolution in each case, despite similar fractal size–number relation for $D_c$ for all the simulations. Rupture can develop only when patches of increasing size (and thus $D_c$) are favorably located so that the cascading process is made possible. Because it is unlikely that such a configuration simultaneously occurs in two (or more) directions, ruptures tend to propagate in a preferential direction (Fig. 4). In terms of rupture velocity, qualitative estimates of its radially averaged value inferred from the rupture front time show little-varying subshear values, consistent with global self-similar properties.

The local variability of the rupture velocity, highlighted by the rough contours of the rupture front, is a direct consequence of rupture interaction with patches of low- or high-$D_c$ values. For a propagation occurring in an area with a given $D_c$-value, rupture accelerates when overlying patches of lower $D_c$ values are broken. This acceleration is even more significant when the decrease of $D_c$ is large, although it remains more local because low $D_c$ values are located on relatively smaller patches. An example can be seen in simulation 12 of Figure 4. About 6 s after the initiation, the rupture front is locally distorted due to break of a $D_{c5}$ patch, whereas the rest of the rupture

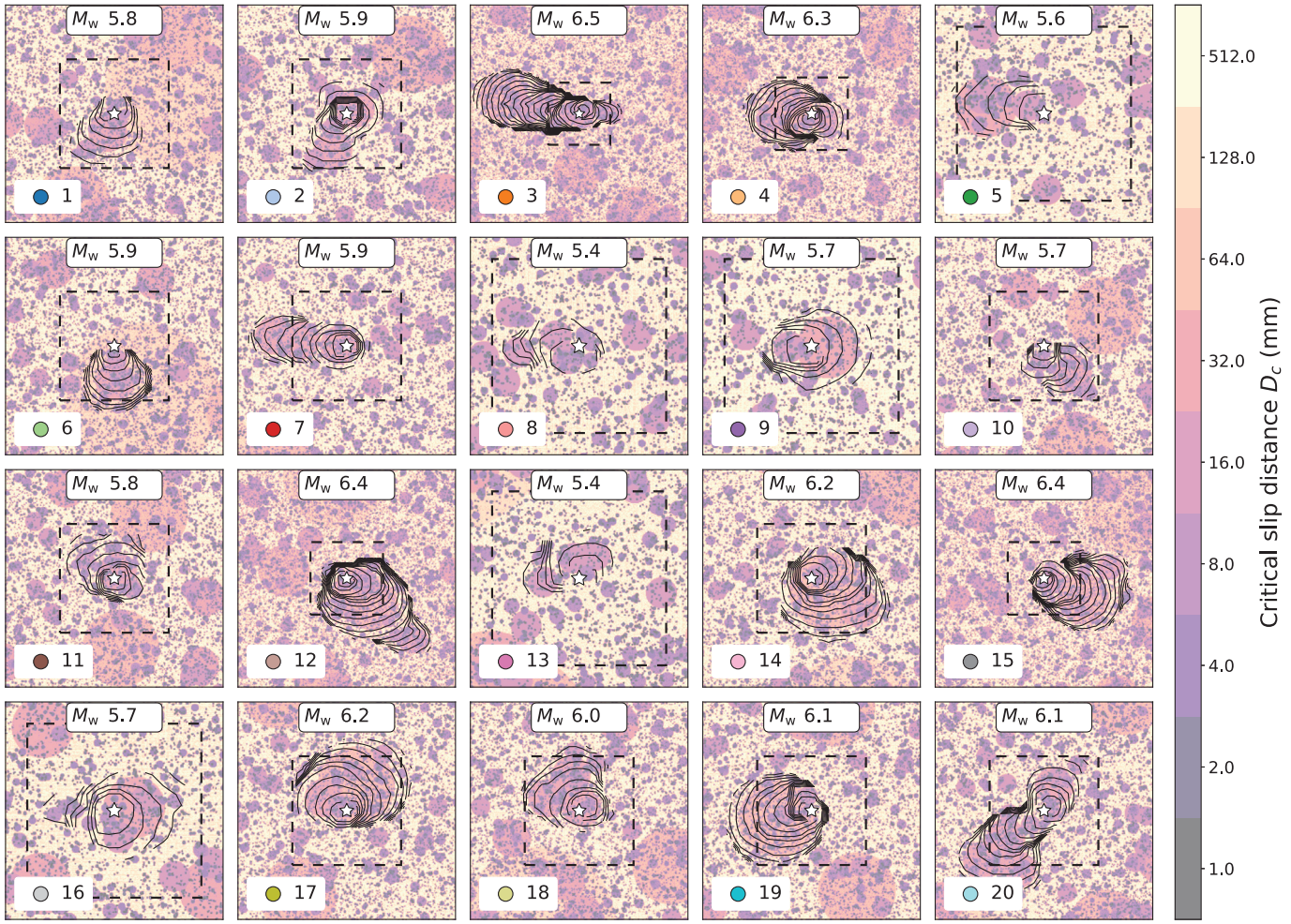


**Figure 4.** Rupture process on 20 $D_c$ random heterogeneity maps leading to large events. The black lines show the contours of the rupture front every 0.5 s. The subspace with physical dimension of 16.384 × 16.384 km is represented by the square delimited by dotted lines. The white star is the position of the rupture initiation and moment magnitude $M_w$ is indicated at the top. Each simulation is numbered and the colored circle at the bottom left refers to the corresponding source time function (STF) in Figure 6.

is mostly controlled by $D_{c\,\max}$. Local increase of $D_c$ leads in contrast to rupture deceleration, as for example in simulation 8 of Figure 4: from 0.5 s after rupture initiation, small patches are in direct contact with $D_{c\,\max}$ areas, which temporarily impedes rupture to go further right. These particular simulations are also shown in Figures S12 and S13. Such positive and negative local variations are caused by random patch position and are therefore balanced over the rupture process. This explains why at the scale of the whole fault, rupture velocity does not diverge from classically observed subshear values.

Figure 5 shows the same 20 simulations with their rupture front contours (as in Fig. 4), but with color scale now showing the maximum slip velocity. As expected from a simple crack model, maximum slip velocity tends to increase with distance from hypocenter, and thus take higher values for the largest events that propagate further. More interestingly, maximum slip velocity often coincides with large ruptured surface (see e.g., simulations 12 or 20, also shown in Figures S14 and S15), implying that maximum slip velocity correlates with local rupture velocity, which has also been pointed out by other dynamic studies (Schmedes *et al.*, 2010; Bizzarri, 2012). The role of $D_c$ in this correlation is even more explicit than for rupture velocity (Fig. 4), because maximum slip velocity areas in Figure 5 mimic the circular shape of the patches.

## Effects on STFs

Local correlation between slip and rupture velocity is expected to be reflected in the STF characteristics. The moment rate $\dot{M}(t)$ described by the STF is defined by

$$\dot{M}(t) = \mu \int_{S(t)} \dot{u}(\boldsymbol{r}, t)\, dS, \tag{3}$$

in which $\mu$ is the rigidity, $\dot{u}(\boldsymbol{r}, t)$ is the slip velocity at time $t$ and position $\boldsymbol{r}$, and $S(t)$ is the surface area ruptured between origin time and time $t$. Equation (3) shows that a rapid increase of $S(t)$ (corresponding to a high local rupture velocity), associated

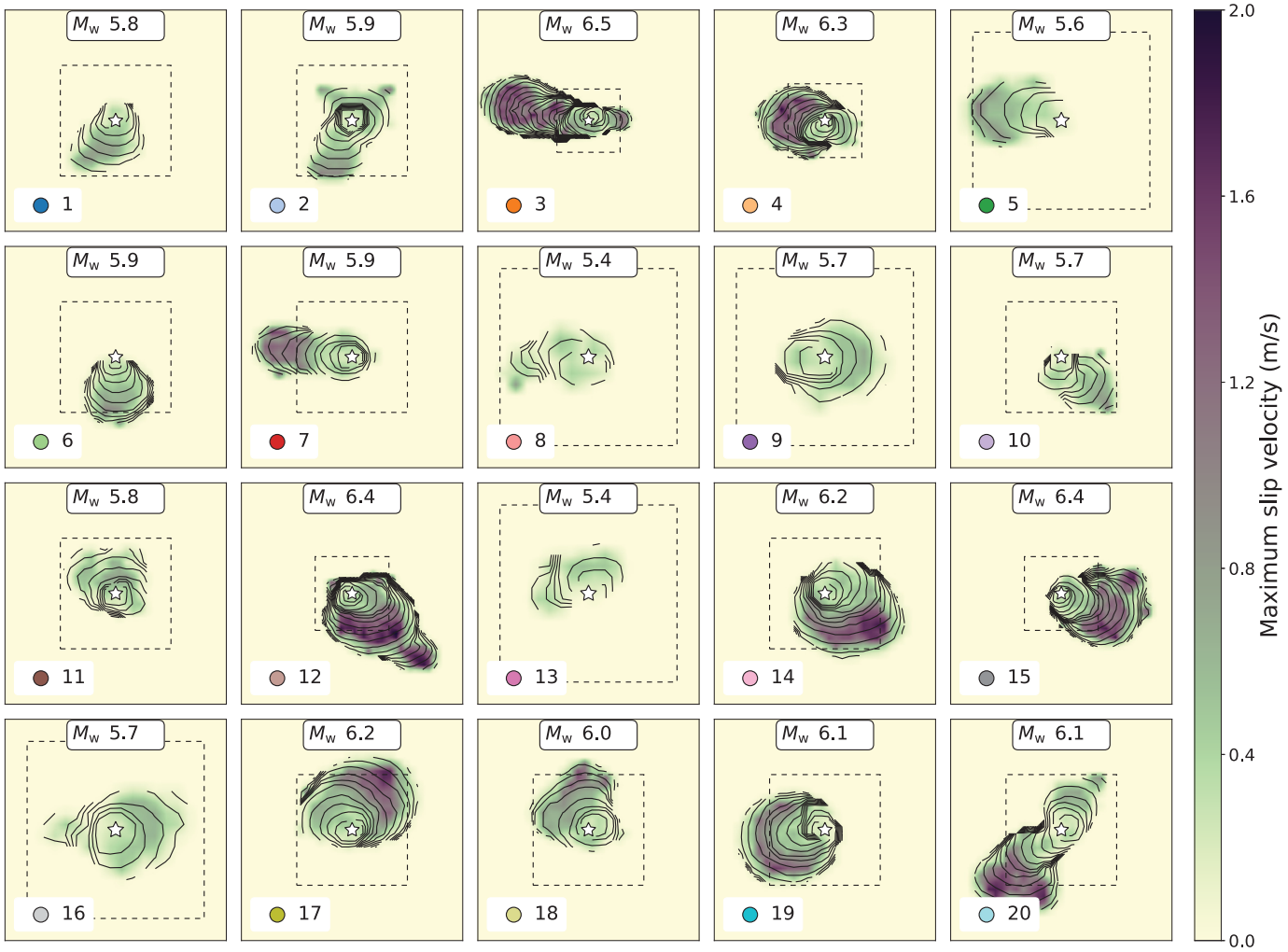


**Figure 5.** Slip velocity maps of the same 20 events as in Figure 4. The black lines represent the contours of the rupture front every 0.5 s. The subspace with physical dimension of 16.384 × 16.384 km is represented by the square delimited by dotted lines. The white star is the position of the rupture initiation and moment magnitude $M_w$ is indicated at the top. Each simulation is numbered and the colored circle at the bottom left refers to the corresponding STF in Figure 6.

with a large-slip velocity on this newly ruptured surface area, create a burst in the STFs. Reciprocally, observed STFs therefore have the potential to quantify the realism of the dynamic scenarios generated by heterogeneous $D_c$ distribution.

For each simulation, we apply a three-point symmetric moving average on the local slip velocity time functions, before computing the synthetic STFs using equation (3). Such smoothing allows to get rid from possible numerical instabilities at high frequencies (>2 Hz) and takes into account that such frequencies are anyway depleted in the observed STFs. Besides, we also verified that we get the same results with raw simulated STFs. About 20 simulated STFs are shown in Figure 6, color coded as indicated in Figure 4. In agreement with global scaling laws, their duration and peak moment rate tend to increase with magnitude. However, diversity for events of similar magnitude is also observed, in particular in the time at which STFs grow toward their maximum. Such immediate or delayed accelerations are observed for real earthquakes (a classical example of delayed rupture is the 2014 $M_w$ 8 Iquique earthquake (Yagi *et al.*, 2014; Gusman *et al.*, 2015). These results are also in qualitative agreement with duration variability found in real STF catalogs (Houston, 2001; Bilek *et al.*, 2004; Courboulex *et al.*, 2016; Chounet and Vallée, 2018).

Besides variability in their macroscopic properties, local features also differ from STF to STF, as a consequence of rupture and slip velocity distribution. At a given time, rupture can be almost stopped (like in the simulation 3 shown in orange at a time of 5 s), or in full development due to an increase in rupture velocity and slip velocity (like in the simulation 15 shown in gray, see also Fig. S16). This individual complexity differs from models with continuous features such as $D_c \propto d$, with $d$ is the hypocentral distance (Aochi and Ide, 2004). The latter configuration leads to a steady growth of the moment rate with $\dot{M}(t) \propto t^2$, as for the rupture dynamics of a self-similar circular crack with constant stress drop and rupture velocity (Kostrov,

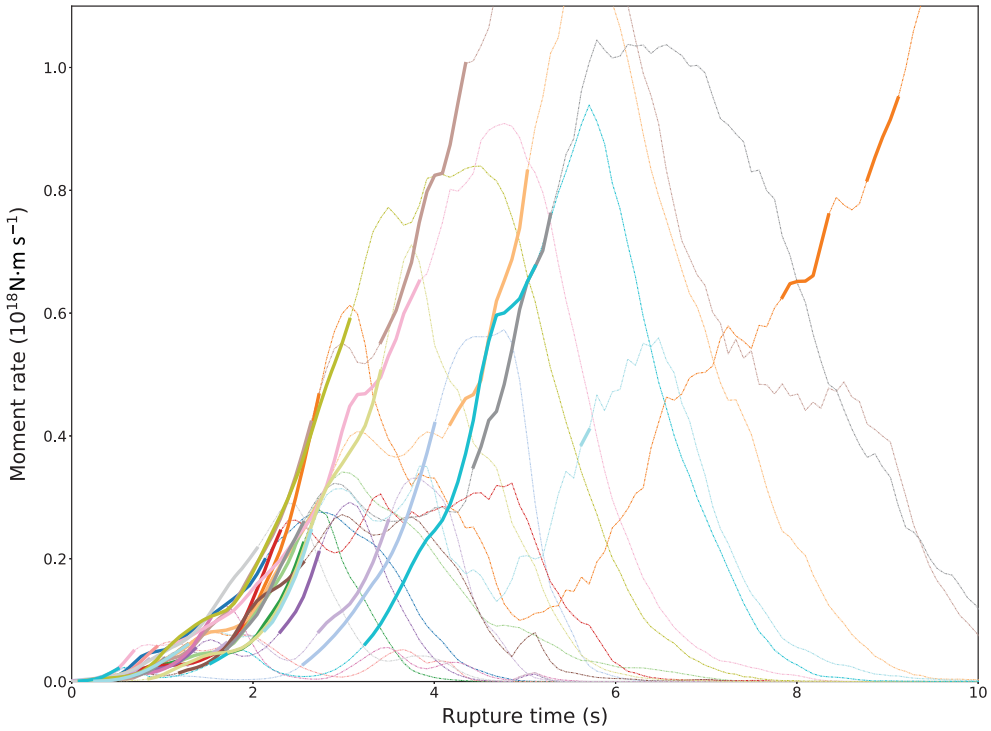


**Figure 6.** STFs of the same 20 events as in Figures 4 and 5. Each STF can be associated with the corresponding event using the color code of Figures 4 and 5. The thick colored part of each STF is the development phase as defined in Renou *et al.* (2019).

1964; Dahlen, 1974; Madariaga, 1976; Nielsen and Madariaga, 2003).

## Comparison with observed development phase of STFs

To compare synthetics STFs with the real ones, one approach is to compute the statistical deviation from the $t^2$ self-similar development in both cases. Such a quantification has to take into account the possible delays before main rupture activation, as well as nonmonotonic features of the STFs. Using STFs from SCARDEC catalog, Renou *et al.* (2019) overcome these difficulties by characterizing how rupture accelerates independently of when it accelerates. To do so, the growing parts preceding the peak moment rate are considered and are hereafter referred to as the development phase. The STF slope computation at prescribed moment rates then allows to retrieve a generic time evolution of the moment rate inside the development phase. Full details of the method are described in the sections 2 and 3 of Renou *et al.* (2019), and comparison between their observational evidence and the results for our simulations are presented in the following paragraphs.

We apply their method for the simulated STFs and show the development phases with thick colored lines in Figure 6. Development phases exhibit similar increase of the moment rate, due to the fact that they are by model construction controlled by the propagation into the same series of hierarchical patches, but their timings are significantly different. Besides being consistent with early and delayed development phases observed in real STFs, such feature is consistent with the first results of Renou *et al.* (2019): moment acceleration values (i.e., local slope of the STF) for a given moment rate are on average magnitude independent within the development phase.

The second result of the study of Renou *et al.* (2019) reveals that on average, moment rate $\dot{M}_d$ during the development phase follows a power law $\dot{M}_d \propto t^{n_d}$ with $n_d = 2.7 \pm 0.11$. We adopt the same method to retrieve $n_d$ for the simulated development phases, by extracting local slopes at prescribed moment rates $(\dot{M}_d)_i (i = 1, 30)$ from $10^{15}$ to $10^{18}$ N · ms$^{-1}$ (Fig. 7). A linear fit in log–log scale is derived from these individual moment acceleration values and is represented in Figure 7 with the red line. The relation found from observations is added (black dashed line), computed for larger moment rate values as SCARDEC catalog contains STFs from larger earthquakes. The slopes $m$ of these two linear fits, related to $n_d$ as $n_d = \frac{1}{1-m}$, are equal to 0.63 and 0.65 for observations and simulations, respectively. Although the small number of simulations prevents robust statistical significance for values of linear coefficients, it is clear that the $m = 0.65$ value is significantly higher than self-similar law would predict ($m = 0.5$, black dashed–dotted line).

From a mechanical perspective, our results suggest that at the beginning of the rupture process, the energy balance around the rupture front can be equilibrated to grow up quasi steady. Rupture propagates on small patches with low $D_c$ and overlying patches with lower $D_c$ are too small to drastically perturb the moment rate evolution. However, earthquake rupture finds at some point a favorable patch of relatively important size and over which smaller patches with low $D_c$ are present. In this case, rupture accelerates in terms of slip velocity and rupture velocity and generates moment rate accelerations similar to the observations. Such accelerations do not exist in a purely self-similar model. It is therefore important to establish a model for which the rupture starts as a cascade and is

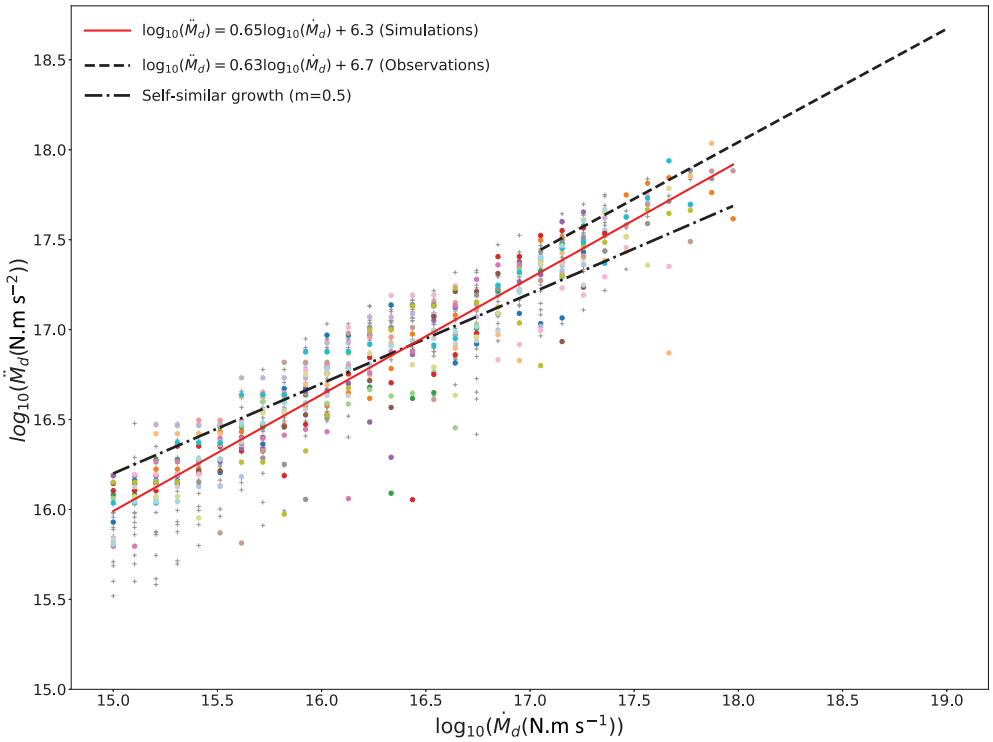


**Figure 7.** Moment acceleration as a function of moment rate in the development phase. Moment acceleration values are color coded to be identified with the corresponding STFs of Figure 6 and are used to compute the linear fit in red. Values from additional simulations are indicated by gray crosses. The black dashed line is the linear fit based on observational data (Renou *et al.*, 2019). The black dashed–dotted line is the best fit assuming a self-similar growth (slope $m = 0.5$).

governed after some point by a characteristic patch, including heterogeneity within, which also controls the final earthquake size.

## EFFECTS OF A RANDOM INITIAL STRESS FIELD

In the previous section, the STFs properties were fully governed by heterogeneous $D_c$. However, while its exact distribution before earthquakes cannot be inferred, initial stress field on real faults is variable at all scales and also generates complexity of the rupture process (Hanks, 1979; Andrews, 1980, 1981). We generate maps of heterogeneous initial stress fields following the approach of Ripperger *et al.* (2007), in which the high-wavenumber amplitude content of a random field $R$ is attenuated by a power law decay. In this model, the 2D spatial Fourier transform of the initial stress $\tau_0(k_x, k_y)$ takes the form:

$$\tau_0(k_x, k_y) = \begin{cases} \overline{\tau_0} + A\ R(k_x, k_y) & \text{if } k \le k_c \\ \overline{\tau_0} + \frac{A\ R(k_x, k_y)}{(k/k_c)^{\gamma}} & \text{if } k > k_c \end{cases}, \qquad (4)$$

in which $k_x$ and $k_y$ are the wavenumber components in the two spatial directions, $k = \sqrt{k_x^2 + k_y^2}$, $k_c = 2\pi/L_c$ is the wavenumber (associated with a correlation length $L_c$) beyond which spectral amplitude decreases, and $\gamma$ is the power of the decay.

The average initial stress value $\overline{\tau_0}$ takes the same value as in the homogeneous case (3 MPa) and we adapt the constant $A$ so that $\tau_0$ maximum values do not exceed $\tau_y = 5$ MPa. The same spectral description is used for each of the four subspaces in order they have the same heterogeneity at all scales, meaning that $L_c$ is relative to the length $L$ of each subspace.

For each of the previous 40 heterogeneous $D_c$ maps, simulations are now performed on random heterogeneous maps of $\tau_0$, and we extract the largest ruptures that naturally stop before reaching the borders of the fault model. Four configurations are tested using $\gamma \in \{1, 2\}$ and $L_c \in \{L/4, L\}$ (see the supplemental material). An example is shown in Figure 8, in which the heterogeneous $D_c$ map of simulation 12 (see Fig. 4) is combined with the four $\tau_0$ configurations. In addition to the location of small patches of low-$D_c$ values, preferential direction of propagation is now also governed by areas of high-$\tau_0$ values as it is closer to $\tau_y$, hence requiring less stress accumulation to propagate dynamic instability.

A feature that was not found in simulations with homogeneous $\tau_0$ is the dynamic triggering at distance away from the main rupture front for some simulations, mimicking the behavior observed in some earthquake kinematic models (Freymueller *et al.*, 1994; Meng *et al.*, 2018). However, in all cases shown in Figure 8 and in the supplemental figures, we observe that the spatial variations of $\tau_0$ do not strongly affect rupture propagation, which is mainly influenced by heterogeneous $D_c$. The weak effect of $\tau_0$ variability is consistent with theoretical considerations, as pointed out by Ripperger *et al.* (2007): "…whereas $G_c$ enters the "crack tip equation of motion", by its local value, stress drop contributes as a weighted spatial average through the integral defining the stress intensity factor." This integral value of the stress drop for short-scale $\tau_0$ variations and constant residual stress is therefore close to the mean value of the random distribution, explaining why simulations resemble the ones obtained for homogeneous $\tau_0$.

Fits of the moment acceleration as a function of the moment rate during development phase are computed for the four cases

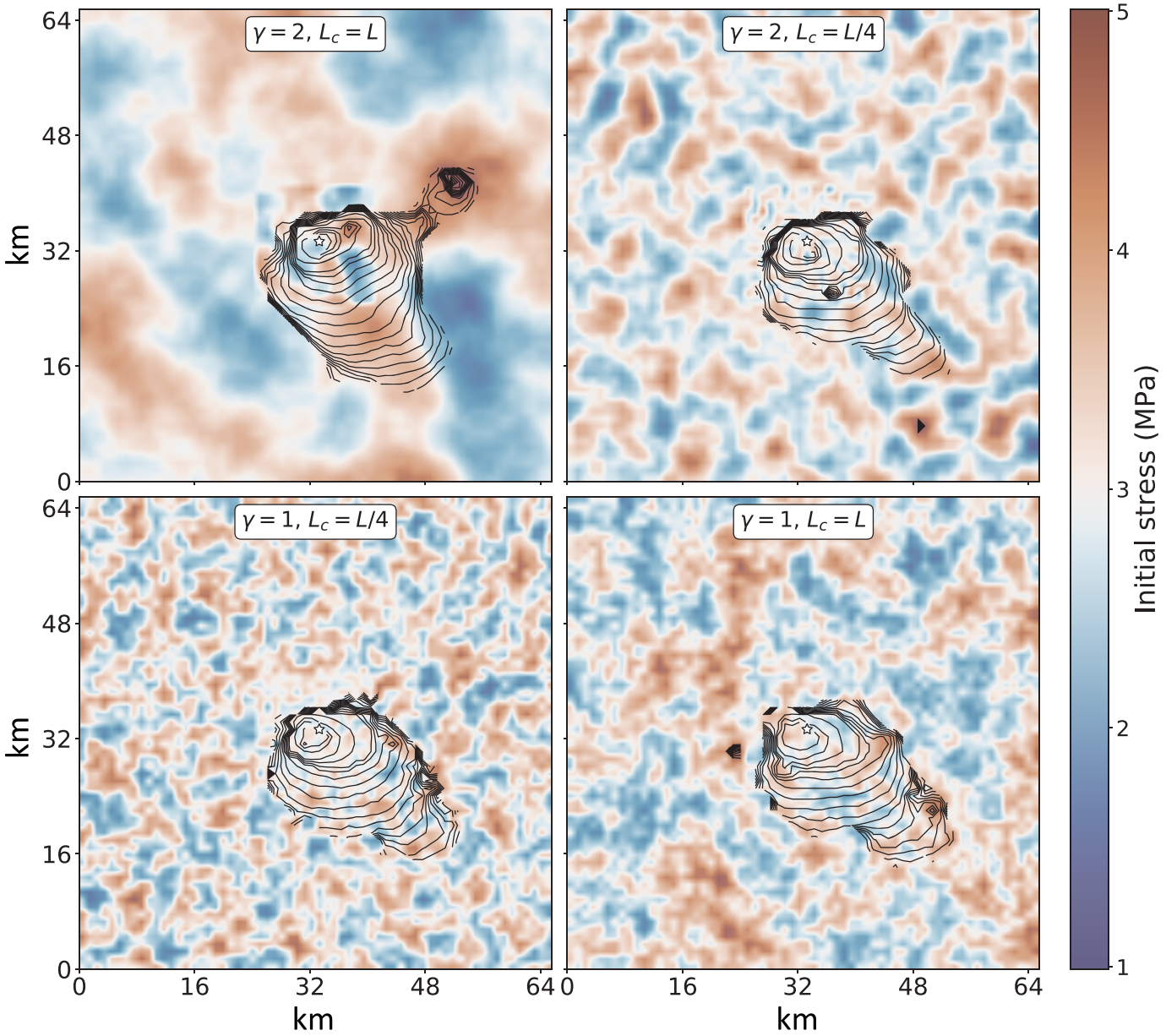


(see the supplemental material), and we observe that the increase is similar to the one determined in Figure 6, suggesting that heterogeneous $\tau_0$ has a less drastic effect on the slope $m$ than heterogeneous $D_c$. To further document this point, we also considered a fault with heterogeneous $\tau_0$ and continuous linear increase of $D_c$ with hypocentral distance. As shown in supplemental material (Figs. S10 and S11), it confirms that for values bounded between 0 and 5 MPa, $\tau_0$ has almost no effect on the rupture propagation as moment rate in the development phase is similar to the $t^2$ self-similar behavior. In the present configuration, larger variability is not possible to keep $\tau_0$ below the peak strength $\tau_y$. However, we can infer that larger extreme values for $\tau_0$ would have more impact, as shown in the studies of Danré *et al.* (2019) and Yin *et al.* (2021). But in our model, this would lead in turn to modify both $\tau_y$-value and the evolution of $D_c$ as a function of the patch size.

**Figure 8.** Examples of heterogeneous initial stress maps for different values of $\gamma$ and $L_c$ (see equation 4), combined with the heterogeneous $D_c$ map of simulation 12 in Figure 4. The black lines represent the contours of the rupture front every 0.5 s. 11

## CONCLUSION

The hierarchical slip-weakening distance $D_c$ model of Aochi and Ide (2004) and Ide and Aochi (2005) had been shown to reproduce the macroscopic properties of earthquakes, such as size-frequency distribution or magnitude-duration scaling laws. We show in this study that this model is also able to reproduce characteristics internal to the rupture process, and in particular the way it accelerates. Although having a large variability (particularly in the timing at which seismic rupture efficiently develops), the growing phase of the observed STFs

follows an empirical power law that departs from standard self-similar models: rather than growing quadratically with time, Renou *et al.* (2019) found a larger time exponent of 2.7. The dynamics of the hierarchical $D_c$ model reproduces this behavior as it creates local correlations of the slip and rupture velocities, resulting in local increases of the STF slope.

In terms of ground-motion prediction, these sharp parts of the STFs are expected to play an important role. As a matter of fact, in a far-field point-source configuration, ground acceleration is the second derivative of the STF, which largely enhances the role of the high-frequency bursts. Correlation between ground velocity and seismic moment acceleration therefore implies that the transient episodes shown in this study have an impact on peak ground velocity values. Even if a highly heterogeneous initial stress field may have a role, our simulations show that the observed behavior can be obtained using only variability in the friction parameters.

## DATA AND RESOURCES

Simulation code of the multiscale dynamic rupture propagation can be downloaded online at https://github.com/aochihi/. Observed source time functions (STFs) used in this study are from the SCARDEC database publicly available at http://scardec.projects.sismo.ipgp.fr/. The supplemental material first include Figure S1, showing the consistent self-similar relation between seismic moment and time of the peak moment rate for a large number of simulations. Four heterogeneous initial stress configurations not included in the main text, and the associated moment acceleration as a function of moment rate for 20 simulations, are shown in Figures S2–S9. Figures S10 and S11 show the case of heterogeneous initial stress field together with linear increase of $D_c$ with hypocentral distance. Figures S12–S15 provide a closer look to some simulations shown in Figures S4 and S5. Figure S16 further documents the relation between high-frequency radiated energy and joint increase of slip and rupture velocities.

## DECLARATION OF COMPETING INTERESTS

The authors acknowledge that there are no conflicts of interest recorded.

## ACKNOWLEDGMENTS

The authors thank the two anonymous reviewers, as well as Martin Mai and Luis Dalguer (Editor-in-Chief and Associate Editor), for their constructive comments and remarks on this study. Discussions with Pascal Bernard, Claudio Satriano, and Alexandre Schubnel also helped improve the initial article.

## REFERENCES

Abercrombie, R. E., and J. R. Rice (2005). Can observations of earthquake scaling constrain slip weakening? *Geophys. J. Int.* **162,** no. 2, 406–424.

Aki, K. (1967). Scaling law of seismic spectrum, *J. Geophys. Res.* **72,** no. 4, 1217–1231.

Andrews, D. (1980). A stochastic fault model: 1. Static case, *J. Geophys. Res.* **85,** no. B7, 3867–3877.

Andrews, D. (1981). A stochastic fault model: 2. Time-dependent case, *J. Geophys. Res.* **86,** no. B11, 10,821–10,834.

Aochi, H., and S. Ide (2004). Numerical study on multi-scaling earthquake rupture, *Geophys. Res. Lett.* **31,** no. 2, L02606 .

Aochi, H., and C. Twardzik (2020). Imaging of seismogenic asperities of the 2016 ml 6.0 amatrice, Central Italy, earthquake through dynamic rupture simulations, *Pure Appl. Geophys.* **177,** no. 5, 1931–1946.

Aochi, H., E. Fukuyama, and M. Matsu'ura (2000). Spontaneous rupture propagation on a non-planar fault in 3-D elastic medium, *Pure Appl. Geophys.* **157,** nos. 11/12, 2003–2027.

Aso, N., R. Ando, and S. Ide (2019). Ordinary and slow earthquakes reproduced in a simple continuum system with stochastic temporal stress fluctuations, *Geophys. Res. Lett.* **46,** no. 24, 14,347–14,357.

Bilek, S., T. Lay, and L. Ruff (2004). Radiated seismic energy and earthquake source duration variations from teleseismic source time functions for shallow subduction zone thrust earthquakes, *J. Geophys. Res.* **109,** no. B9, doi: 10.1029/2004JB003039.

Bizzarri, A. (2012). Rupture speed and slip velocity: What can we learn from simulated earthquakes? *Earth Planet. Sci. Lett.* **317,** 196–203.

Chounet, A., and M. Vallée (2018). Global and interregion characterization of subduction interface earthquakes derived from source time functions properties, *J. Geophys. Res.* **123,** no. 7, 5831–5852.

Chounet, A., M. Vallée, M. Causse, and F. Courboulex (2018). Global catalog of earthquake rupture velocities shows anticorrelation between stress drop and rupture velocity, *Tectonophysics* **733,** 148–158.

Cocco, M., E. Tinti, C. Marone, and A. Piatanesi (2009). Scaling of slip weakening distance with final slip during dynamic earthquake rupture, *Int. Geophys.* **94,** 163–186.

Courboulex, F., M. Vallée, M. Causse, and A. Chounet (2016). Stress-drop variability of shallow earthquakes extracted from a global database of source time functions, *Seismol. Res. Lett.* **87,** no. 4, 912–918.

Dahlen, F. (1974). On the ratio of P-wave to S-wave corner frequencies for shallow earthquake sources, *Bull. Seismol. Soc. Am.* **64,** no. 4, 1159–1180.

Danré, P., J. Yin, B. P. Lipovsky, and M. A. Denolle (2019). Earthquakes within earthquakes: Patterns in rupture complexity, *Geophys. Res. Lett.* **46,** no. 13, 7352–7360.

Denolle, M. A. (2019). Energetic onset of earthquakes, *Geophys. Res. Lett.* **46,** no. 5, 2458–2466.

Eshelby, J. (1969). The elastic field of a crack extending non-uniformly under general anti-plane loading, *J. Mech. Phys. Solids* **17,** no. 3, 177–199.

Freund, L. (1972). Energy flux into the tip of an extending crack in an elastic solid, *J. Elast.* **2,** no. 4, 341–349.

Freymueller, J., N. King, and P. Segall (1994). The co-seismic slip distribution of the landers earthquake, *Bull. Seismol. Soc. Am.* **84,** no. 3, 646–659.

Fukuyama, E., and R. Madariaga (1998). Rupture dynamics of a planar fault in a 3d elastic medium: Rate-and slip-weakening friction, *Bull. Seismol. Soc. Am.* **88,** no. 1, 1–17.

Gallovič, F., L. Valentová, J.-P. Ampuero, and A.-A. Gabriel (2019). Bayesian dynamic finite-fault inversion: 2. Application to the 2016 Mw 6.2 Amatrice, Italy, earthquake, *J. Geophys. Res.* **124,** no. 7, 6970–6988.

Gusman, A. R., S. Murotani, K. Satake, M. Heidarzadeh, E. Gunawan, S. Watada, and B. Schurr (2015). Fault slip distribution of the 2014

Iquique, Chile, earthquake estimated from ocean-wide tsunami waveforms and GPS data, *Geophys. Res. Lett.* **42,** no. 4, 1053–1060.

Hanks, T. C. (1979). *b* values and ω- γ seismic source models: Implications for tectonic stress variations along active crustal fault zones and the estimation of high-frequency strong ground motion, *J. Geophys. Res.* **84,** no. B5, 2235–2242.

Houston, H. (2001). Influence of depth, focal mechanism, and tectonic setting on the shape and duration of earthquake source time functions, *J. Geophys. Res.* **106,** no. B6, 11,137–11,150.

Ida, Y. (1972). Cohesive force across the tip of a longitudinal-shear crack and griffith's specific surface energy, *J. Geophys. Res.* **77,** no. 20, 3796–3805.

Ide, S. (2019). Frequent observations of identical onsets of large and small earthquakes, *Nature* **573,** no. 7772, 112–116.

Ide, S., and H. Aochi (2005). Earthquakes as multiscale dynamic ruptures with heterogeneous fracture surface energy, *J. Geophys. Res.* **110,** no. B11, doi: 10.1029/2004JB003591.

Kaneko, Y., and P. Shearer (2014). Seismic source spectra and estimated stress drop derived from cohesive-zone models of circular subshear rupture, *Geophys. J. Int.* **197,** no. 2, 1002–1015.

Kostrov, B. (1964). Selfsimilar problems of propagation of shear cracks, *J. Appl. Math. Mech.* **28,** no. 5, 1077–1087.

Kostrov, B. (1966). Unsteady propagation of longitudinal shear cracks, *J. Appl. Math. Mech.* **30,** no. 6, 1241–1248.

Lancieri, M., R. Madariaga, and F. Bonilla (2012). Spectral scaling of the aftershocks of the Tocopilla 2007 earthquake in northern Chile, *Geophys. J. Int.* **189,** no. 1, 469–480.

Madariaga, R. (1976). Dynamics of an expanding circular fault, *Bull. Seismol. Soc. Am.* **66,** no. 3, 639–666.

Mai, P. M., M. Galis, K. K. Thingbaijam, J. C. Vyas, and E. M. Dunham (2018). Accounting for fault roughness in pseudo-dynamic ground-motion simulations, in *Best Practices in Physics-based Fault Rupture Models for Seismic Hazard Assessment of Nuclear Installations*, Springer, 95–126.

Meier, M.-A., T. Heaton, and J. Clinton (2016). Evidence for universal earthquake rupture initiation behavior, *Geophys. Res. Lett.* **43,** no. 15, 7991–7996.

Meng, L., H. Bao, H. Huang, A. Zhang, A. Bloore, and Z. Liu (2018). Double pincer movement: Encircling rupture splitting during the 2015 Mw 8.3 illapel earthquake, *Earth Planet. Sci. Lett.* **495,** 164–173.

Nielsen, S., and R. Madariaga (2003). On the self-healing fracture mode, *Bull. Seismol. Soc. Am.* **93,** no. 6, 2375–2388.

Nielsen, S., E. Spagnuolo, M. Violay, S. Smith, G. Di Toro, and A. Bistacchi (2016). G: Fracture energy, friction and dissipation in earthquakes, *J. Seismol.* **20,** no. 4, 1187–1205.

Okuda, T., and S. Ide (2018). Hierarchical rupture growth evidenced by the initial seismic waveforms, *Nat. Commun.* **9,** no. 1, 1–7.

Olsen, K., R. Madariaga, and R. J. Archuleta (1997). Three-dimensional dynamic simulation of the 1992 Landers earthquake, *Science* **278,** no. 5339, 834–838.

Renou, J., M. Vallée, and P. Dublanchet (2019). How does seismic rupture accelerate? Observational insights from earthquake source time functions, *J. Geophys. Res.* **124,** no. 8, 8942–8952.

Ripperger, J., J.-P. Ampuero, P. Mai, and D. Giardini (2007). Earthquake source characteristics from dynamic rupture with constrained stochastic fault stress, *J. Geophys. Res.* **112,** no. B4, doi: 10.1029/2006JB004515.

Sato, T., and T. Hirasawa (1973). Body wave spectra from propagating shear cracks, *J. Phys. Earth* **21,** no. 4, 415–431.

Schmedes, J., R. J. Archuleta, and D. Lavallée (2010). Correlation of earthquake source parameters inferred from dynamic rupture simulations, *J. Geophys. Res.* **115,** no. B3, doi: 10.1029/2009JB006689.

Tanioka, Y., and L. J. Ruff (1997). Source time functions, *Seismol. Res. Lett.* **68,** no. 3, 386–400.

Ulrich, T., A.-A. Gabriel, J.-P. Ampuero, and W. Xu (2019). Dynamic viability of the 2016 Mw 7.8 Kaikōura earthquake cascade on weak crustal faults, *Nat. Commun.* **10,** no. 1, 1–16.

Vallée, M., and V. Douet (2016). A new database of source time functions (stfs) extracted from the scardec method, *Phys. Earth Planet. In.* **257,** 149–157.

Vallée, M., J. Charléty, A. M. Ferreira, B. Delouis, and J. Vergoz (2011). Scardec: A new technique for the rapid determination of seismic moment magnitude, focal mechanism and source time functions for large earthquakes using body-wave deconvolution, *Geophys. J. Int.* **184,** no. 1, 338–358.

Wollherr, S., A.-A. Gabriel, and P. M. Mai (2019). Landers 1992 "reloaded": Integrative dynamic earthquake rupture modeling, *J. Geophys. Res.* **124,** no. 7, 6666–6702.

Yagi, Y., R. Okuwaki, B. Enescu, S. Hirano, Y. Yamagami, S. Endo, and T. Komoro (2014). Rupture process of the 2014 Iquique Chile earthquake in relation with the foreshock activity, *Geophys. Res. Lett.* **41,** no. 12, 4201–4206.

Yin, J., Z. Li, and M. A. Denolle (2021). Source time function clustering reveals patterns in earthquake dynamics, *Seismol. Res. Lett.* **92,** no. 4, 2343–2353.

**Manuscript received 15 August 2021**